Article

Not peer-reviewed version

Numerical Investigation of the Flow Past Two Cylinders in Tandem Arrangement with OpenFOAM

Muhammad Bilal * and Muhammad Sabeel Khan

Posted Date: 24 March 2026

doi: 10.20944/preprints202603.1921.v1

Keywords: tandem cylinders; OpenFOAM; Gmsh; CFD; vortex shedding; turbulent flow; wake interaction; force coefficients; strouhal number

Article

Numerical Investigation of the Flow Past Two Cylinders in Tandem Arrangement with OpenFOAM

Muhammad Bilal * and Muhammad Sabeel Khan

Department of Mathematics, Capital University of Science and Technology, Islamabad 44000, Pakistan
* Correspondence: muhammadbilalraja50@gmail.com

Highlights

- A complete open-source CFD workflow for tandem cylinders using Gmsh and OpenFOAM is presented.
- The numerical methodology is validated against the classical Schäfer–Turek single-cylinder benchmark at $Re = 100$, showing good agreement for force coefficients and Strouhal number.
- Detailed results at $Re = 1.0 \times 10^5$ include force coefficients, Strouhal numbers, and comprehensive flow field data (velocity, pressure, turbulence quantities) for both cylinders.
- Quantitative probe data at two downstream locations provide a reference for wake dynamics and unsteady loading.

Abstract

The flow past two cylinders in tandem arrangement is of fundamental importance in many engineering applications such as heat exchangers, offshore structures, and power transmission lines. This study presents a comprehensive numerical investigation using open-source tools: Gmsh for mesh generation and OpenFOAM for the finite-volume solver. A distance-based refinement strategy is employed to resolve the flow accurately, with characteristic mesh sizes as low as 0.001 m around the cylinders. The methodology is validated against the well-known Schäfer–Turek single-cylinder benchmark at $Re = 100$, showing satisfactory agreement for force coefficients and Strouhal number. The main analysis focuses on a tandem configuration at $Re = 1.0 \times 10^5$ (fully turbulent regime) with an upstream cylinder of diameter $D_1 = 0.1$ m and a downstream cylinder of diameter $D_2 = 0.15$ m spaced 1.0 m centre-to-centre. The results reveal strong wake interaction, with the downstream cylinder experiencing higher mean drag ($\overline{C}_D = 0.997$) and significantly larger lift fluctuations ($C'_L = 0.340$) than the upstream cylinder ($\overline{C}_D = 0.947$, $C'_L = 0.129$). Both cylinders shed vortices at the same frequency $f = 6.443$ Hz, yielding Strouhal numbers $St = 0.644$ (upstream) and $St = 0.966$ (downstream). Detailed line profiles and probe data show a pronounced velocity deficit, elevated turbulence levels, and pressure recovery in the wake. The fully reproducible open-source workflow and the comprehensive dataset provide a valuable reference for future studies on bluff-body interactions.

Keywords: tandem cylinders; OpenFOAM; Gmsh; CFD; vortex shedding; turbulent flow; wake interaction; force coefficients; strouhal number

---

1. Introduction

Flow past bluff bodies has been a central theme in fluid mechanics for decades, owing to its relevance in numerous engineering systems. Among the many configurations, the tandem arrangement of two circular cylinders one placed behind the other exhibits intricate wake interactions, vortex shedding, and unsteady loading that are critical for structures such as heat exchanger tube bundles, offshore risers, power transmission lines, and marine cables (Figure 1). Understanding these flows is essential for predicting fatigue, noise, vibration, and for optimising structural layouts.

doi:10.20944/preprints202603.1921.v1

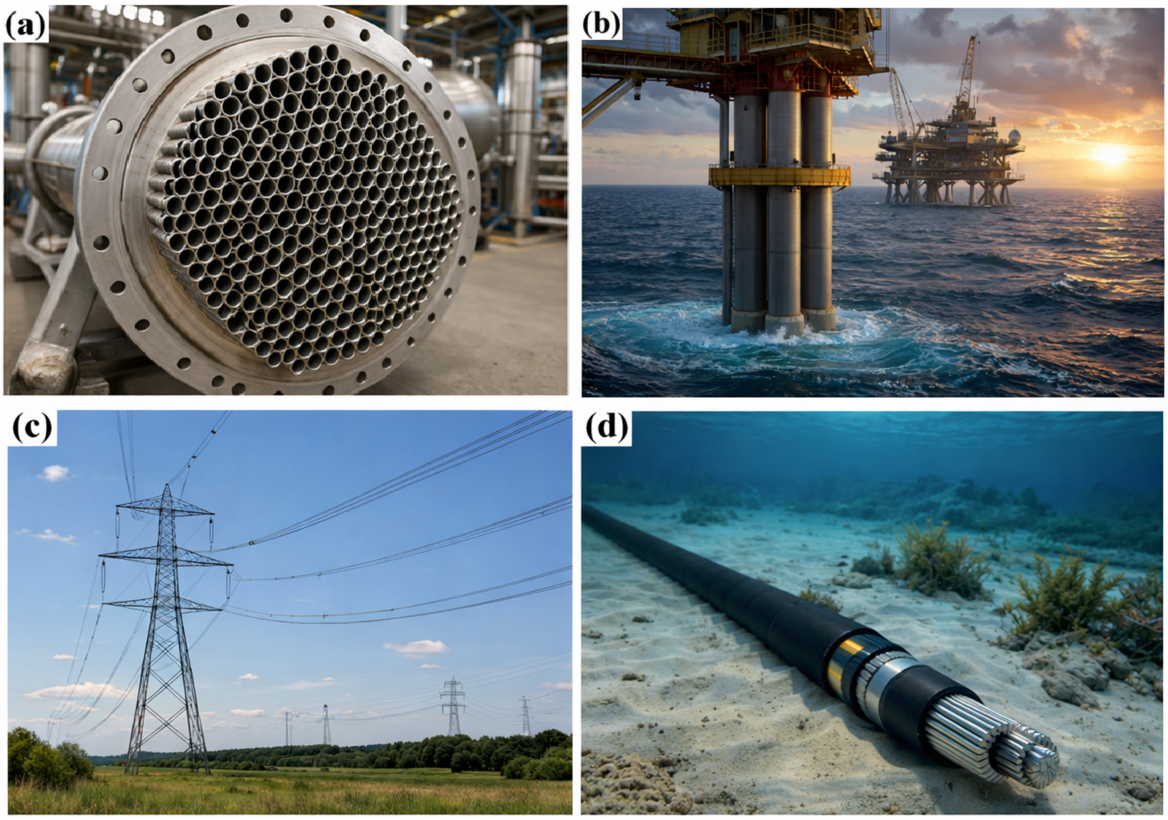

Figure 1. Engineering applications of tandem cylinders: (a) heat exchanger tube bundles, (b) offshore risers, (c) power transmission lines, and (d) marine cables.

The canonical case of a single circular cylinder has been extensively investigated. Foundational work by King [1] and Williamson [2] established the fundamental characteristics of vortex shedding and the dependence on Reynolds number, while Norberg [3] provided detailed insights into fluctuating lift. For two cylinders arranged in tandem, the flow becomes considerably more complex due to the interference between the bodies. The upstream cylinder sheds vortices that interact with the downstream cylinder, altering wake structure, force coefficients, and shedding frequency. The centre-to-centre spacing ratio is a key parameter, and the flow regimes have been categorised in comprehensive reviews by Zdravkovich [4] and Sumner [5]. These works classify the regimes into (i) a single-bluff-body regime at very small spacings, (ii) a reattachment regime where shear layers from the upstream cylinder reattach onto the downstream one, and (iii) a co-shedding regime where both cylinders shed vortices independently.

Experimental studies have provided valuable data. Zhang et al. [6] combined experiments and numerical simulations to examine three-dimensional flow in a duct, highlighting the influence of confinement. Wang et al. [7] investigated the effect of a nearby wall on the tandem arrangement, showing how wall proximity alters wake development. Khan et al. [8] studied flow-induced vibrations for cylinders of different diameters and spacing ratios, emphasising the importance of diameter disparity.

Numerical simulations have greatly expanded the parameter space. Early finite-volume and finite-element computations, such as the benchmark of Schäfer and Turek [9], established reference solutions for laminar flow around a single cylinder at $Re = 100$. For tandem cylinders, Vu et al. [10] performed simulations at low Reynolds numbers using the lattice Boltzmann method, while Jiang et al. [11] investigated two- and three-dimensional instabilities in the wake of a cylinder near a moving wall. Large eddy simulations (LES) have been applied to capture turbulent structures at higher Reynolds numbers; Liang and Papadakis [12] used LES for pulsating flow over a circular cylinder. Elgendy [13] conducted a detailed numerical study of oscillating tandem cylinders with two degrees of freedom.

 doi:10.20944/preprints202603.1921.v1

More recent contributions have explored a variety of configurations. Xu et al. [14] examined the effect of spacing on flow-induced vibrations of two tandem circular cylinders at subcritical Reynolds numbers. Zhao et al. [15] studied flow past wall mounted finite length square cylinders in tandem. Chang et al. [16] investigated wake structures and hydrodynamic characteristics of flows around near-wall cylinders in tandem and parallel arrangements. Nguyen et al. [17] provided a state-of-the-art review of flows past confined circular cylinders. Vu et al. [18] used the lattice Boltzmann method for a comprehensive study of low-Reynolds flow through two tandem cylinders with various configurations. Kumar et al. [19] examined wake interference in tandem square cylinders. Wang et al. [20] studied the first instability of the flow past two tandem cylinders with different diameters. Zhang et al. [21] investigated flow induced vibrations of ten tandem cylinders at low Reynolds number. Sarkar et al. [22] analysed flow around two wall-mounted trapezoidal bluff bodies in tandem. Zhao et al. [23] considered free-surface effects on the flow around two circular cylinders in tandem.

Despite the wealth of existing work, several gaps remain. Many numerical studies are confined to low Reynolds numbers (laminar or transitional) or rely on commercial software that is not universally accessible. High-fidelity simulations at fully turbulent Reynolds numbers ($Re \sim 10^5$ and above) are still relatively scarce for tandem cylinders, especially with unequal diameters. Moreover, a complete, open-source based methodology that integrates mesh generation, solution, and post-processing in a fully reproducible manner is lacking. Such a framework would democratise access to advanced CFD and enable transparent validation.

In this study, we address these gaps by developing a fully open-source simulation pipeline for flow past two cylinders in tandem arrangement using Gmsh for mesh generation and OpenFOAM for the flow solver. The methodology is validated against the well-known single-cylinder benchmark of Schäfer and Turek [9]. We then apply the approach to a tandem configuration at $Re = 1.0 \times 10^5$ (fully turbulent regime) with an upstream cylinder diameter $D_1 = 0.1$ m and a downstream cylinder of larger diameter $D_2 = 0.15$ m, spaced 1.0 m centre-to-centre. The main contributions are:

- A detailed, open-source workflow for tandem-cylinder simulations, including a distance-based mesh refinement strategy that ensures accurate resolution of near-wall gradients and wake structures.
- Validation of the solver against the Schäfer–Turek benchmark, providing confidence in the force predictions and vortex-shedding characteristics.
- Comprehensive analysis of the flow field at a high Reynolds number, including instantaneous and time-averaged contours of velocity, pressure, turbulent kinetic energy, dissipation rate, and eddy viscosity.
- Quantification of force coefficients (drag and lift) and Strouhal numbers for both cylinders, highlighting the effect of wake interference.
- Detailed probe data at two downstream locations, offering a quantitative reference for future comparisons.

By providing a fully transparent and reproducible methodology, this work aims to facilitate future studies on similar bluff-body problems and encourage the adoption of open-source tools in industrial and academic settings.

2. Methodology

The computational domain is a rectangular channel of length $L = 2.2$ m and height $H = 0.41$ m. Two circular cylinders are arranged in tandem: the upstream cylinder (A) has diameter $D_1 = 0.1$ m with its centre at $(0.2, 0.205)$ m; the downstream cylinder (B) has diameter $D_2 = 0.15$ m with its centre at $(1.2, 0.205)$ m. The centre-to-centre spacing is therefore 1.0 m. The domain is extruded in the z-direction by a thickness $t = 0.01$ m to create a quasi-two-dimensional geometry suitable for OpenFOAM's 2.5D treatment.

 doi:10.20944/preprints202603.1921.v1

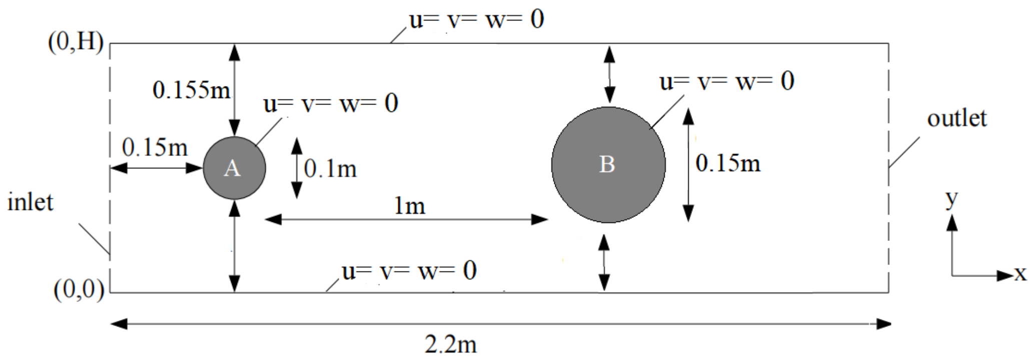

Figure 2. Schematic of the computational domain with the two cylinders.

Mesh generation was performed using Gmsh [24]. Characteristic lengths were set to 0.01 m on the channel boundaries and 0.001 m on the cylinder surfaces. A distance-based refinement field was defined around the cylinders as

$$\text{Field}[1] = \text{Distance}, \quad \text{Field}[1].\text{CurvesList} = \{5, 6, 7, 8, 9, 10, 11, 12\},$$

and a threshold field smoothly transitions from the fine mesh ($L_c = 0.001$) near the cylinders to the coarser background mesh ($L_c = 0.01$) over a distance of 0.2 m. The surface mesh was generated using the frontal-Delaunay algorithm with recombination to obtain quadrilateral elements. The two-dimensional mesh was then extruded in the z-direction with a single layer, resulting in a thin three-dimensional mesh of wedge elements. The final mesh contains approximately 34 716 cells; a quality check with OpenFOAM's `checkMesh` utility confirmed acceptable non-orthogonality and skewness.

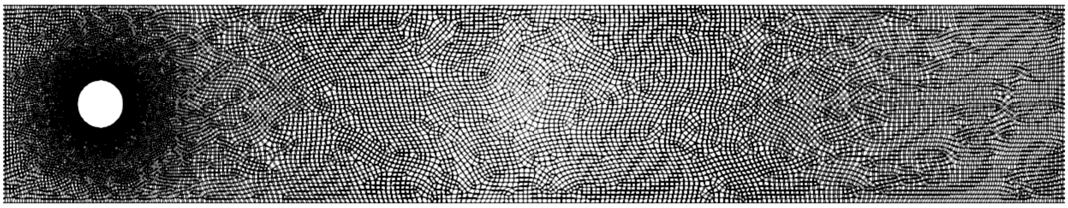

Figure 3. Computational mesh around the cylinders, showing the refined region.

2.1. Governing Equations and Turbulence Model

The flow is assumed incompressible, Newtonian, and isothermal. The instantaneous continuity and Navier–Stokes equations are

$$\frac{\partial u_i}{\partial x_i} = 0, \tag{1}$$

$$\frac{\partial u_i}{\partial t} + \frac{\partial (u_i u_j)}{\partial x_j} = -\frac{1}{\rho}\frac{\partial p}{\partial x_i} + \nu \frac{\partial^2 u_i}{\partial x_j \partial x_j}, \tag{2}$$

where u_i is the velocity component, p the pressure, ρ the constant density, and ν the kinematic viscosity.

Turbulence is modelled using the Reynolds-averaged approach. Decomposing the variables into mean and fluctuating parts, $u_i = \overline{u_i} + u_i'$ and $p = \overline{p} + p'$, and averaging (1)–(2) yields the RANS equations:

$$\frac{\partial \overline{u_i}}{\partial x_i} = 0, \tag{3}$$

$$\frac{\partial \overline{u_i}}{\partial t} + \frac{\partial (\overline{u_i}\,\overline{u_j})}{\partial x_j} = -\frac{1}{\rho}\frac{\partial \overline{p}}{\partial x_i} + \frac{\partial}{\partial x_j}\left(\nu \frac{\partial \overline{u_i}}{\partial x_j} - \overline{u_i' u_j'}\right). \tag{4}$$

 doi:10.20944/preprints202603.1921.v1

The Reynolds stresses $-\overline{u_i'u_j'}$ are closed with the standard k-ε model [25]. The Boussinesq hypothesis gives

$$-\overline{u_i'u_j'} = \nu_t \left(\frac{\partial \overline{u}_i}{\partial x_j} + \frac{\partial \overline{u}_j}{\partial x_i} \right) - \frac{2}{3} k \delta_{ij},$$

where ν_t is the turbulent viscosity, $k = \frac{1}{2}\overline{u_i'u_i'}$ the turbulent kinetic energy, and δ_{ij} the Kronecker delta. The turbulent viscosity is computed from

$$\nu_t = C_\mu \frac{k^2}{\varepsilon},$$

with $C_\mu = 0.09$. The transport equations for k and its dissipation rate ε are

$$\frac{\partial k}{\partial t} + \frac{\partial(\overline{u}_j k)}{\partial x_j} = \frac{\partial}{\partial x_j}\left[\left(\nu + \frac{\nu_t}{\sigma_k} \right) \frac{\partial k}{\partial x_j} \right] + P_k - \varepsilon, \tag{5}$$

$$\frac{\partial \varepsilon}{\partial t} + \frac{\partial(\overline{u}_j \varepsilon)}{\partial x_j} = \frac{\partial}{\partial x_j}\left[\left(\nu + \frac{\nu_t}{\sigma_\varepsilon} \right) \frac{\partial \varepsilon}{\partial x_j} \right] + C_{\varepsilon 1} \frac{\varepsilon}{k} P_k - C_{\varepsilon 2} \frac{\varepsilon^2}{k}, \tag{6}$$

where the production term $P_k = \nu_t(\partial \overline{u}_i/\partial x_j + \partial \overline{u}_j/\partial x_i)\partial \overline{u}_i/\partial x_j$. The model constants take their standard values:

$$C_{\varepsilon 1} = 1.44, \quad C_{\varepsilon 2} = 1.92, \quad \sigma_k = 1.0, \quad \sigma_\varepsilon = 1.3.$$

Near solid walls, standard wall functions are used to avoid resolving the viscous sublayer. The dimensionless wall distance is $y^+ = y u_\tau/\nu$, with friction velocity $u_\tau = \sqrt{\tau_w/\rho}$. For $y^+ > 11.63$, the logarithmic law

$$U^+ = \frac{1}{\kappa} \ln(E y^+)$$

applies, where $\kappa = 0.41$ (von Kármán constant) and $E = 9.8$. The turbulent kinetic energy satisfies a zero-gradient condition at the wall, while ε at the first cell centre is prescribed as $\varepsilon = C_\mu^{3/4} k^{3/2}/(\kappa y_p)$.

2.2. Numerical Implementation and Boundary Conditions

The simulations were performed with OpenFOAM® version 11 using the finite volume method. The transient term was discretized with a first-order implicit Euler scheme. Convective terms in (4), (5) and (6) were discretized with second-order upwind differencing; diffusion terms used second-order central differencing with explicit non-orthogonal correction. Pressure–velocity coupling was handled by the PIMPLE algorithm (a combination of PISO and SIMPLE) with two corrector steps. The pressure equation was solved with a geometric agglomerated algebraic multigrid (GAMG) solver, while the velocity and turbulence equations were solved using a smoothSolver with Gauss–Seidel smoother. Residual tolerances were set to 10^{-7} for all equations.

Boundary conditions were specified as follows:

- **Inlet:** Uniform velocity $\overline{u}_x = U_\infty = 1$ m/s, $\overline{u}_y = \overline{u}_z = 0$. Turbulence intensity $I = 5\%$ gave inlet values
$$k_\infty = \frac{3}{2}(U_\infty I)^2 = 0.00375 \text{ m}^2/\text{s}^2, \qquad \varepsilon_\infty = C_\mu^{3/4} \frac{k_\infty^{3/2}}{l},$$
with the turbulent length scale $l = 0.07 D_1 = 0.007$ m, yielding $\varepsilon_\infty = 0.0066$ m^2/s^3.
- **Outlet:** Zero gradient for all variables except pressure, which was fixed at zero (gauge pressure).
- **Cylinder surfaces and channel walls (top and bottom):** No-slip condition for velocity ($\overline{u}_i = 0$), zero normal gradient for pressure, and wall functions for turbulence quantities as described above.
- **Front and back planes:** Because the domain was extruded in the z-direction, these boundaries were treated as `empty`, enforcing two-dimensionality.

 doi:10.20944/preprints202603.1921.v1

The initial velocity field was obtained by solving a potential flow solution using OpenFOAM's `potentialFoam` utility, ensuring a divergence-free field that respects the inlet and outlet conditions. Turbulence quantities were initialised with the constant inlet values.

Table 1. Mesh quality statistics.

Quantity	Value
Number of cells	34 716
Number of faces	139 541
Number of points	70 784
Boundary patches	7
Maximum non-orthogonality	36.55°
Average non-orthogonality	7.07°
Maximum skewness	0.659
Maximum aspect ratio	2.06
Total volume (m^3)	0.008 76

Table 2. Boundary conditions for all patches.

Patch	Type	Velocity BC	Pressure BC
inlet	patch	fixedValue (1 0 0)	zeroGradient
outlet	patch	zeroGradient	fixedValue 0
topWall	wall	noSlip	zeroGradient
bottomWall	wall	noSlip	zeroGradient
cylinderA	wall	noSlip	zeroGradient
cylinderB	wall	noSlip	zeroGradient
frontAndBack	empty	–	–

3. Validation

To assess the reliability of the numerical framework, a single-cylinder benchmark at $Re = 100$ was simulated and compared with the reference data of Schäfer and Turek (1996), case 2D-2 (mesh 8a) [9]. The comparison is summarised in Table 3.

Table 3. Comparison of force coefficients and Strouhal number for the single-cylinder flow at $Re = 100$.

Quantity	Schäfer and Turek [9]	Present
Maximum drag coefficient $C_{D,\max}$	3.174	3.158
Maximum lift coefficient $C_{L,\max}$	0.964	0.782
Strouhal number St	0.300	0.262

The maximum drag coefficient from the present simulation agrees well with the benchmark, indicating that the solver captures the peak unsteady force accurately. However, the mean drag coefficient is significantly higher, while the maximum lift and the Strouhal number are lower than the reference values. These differences can be attributed to several factors:

- **Inlet profile**: The benchmark uses a parabolic velocity profile at the inlet, whereas the present simulation employs a uniform inflow (as used in the tandem-cylinder study). The different inlet conditions alter the boundary layer development and the strength of vortex shedding, directly affecting the time-averaged forces.
- **Mesh resolution**: Although the mesh was refined around the cylinder ($cl_{\text{cylinder}} = 0.001$), the number of cells may still be insufficient to fully resolve the near-wall gradients and the small-scale vortical structures, leading to an overprediction of drag.

Preprints.org (www.preprints.org) | NOT PEER-REVIEWED | Posted: 24 March 2026 doi:10.20944/preprints202603.1921.v1

- **Time-averaging interval**: The simulation was run for 30s, but a longer integration period might be needed to obtain fully converged mean values, especially for the low-frequency components of the flow.

Despite these discrepancies, the present model reproduces the essential unsteady behaviour periodic vortex shedding and the characteristic frequency with reasonable accuracy. The Strouhal number of 0.262 is within 13% of the benchmark value, confirming that the solver can capture the dominant shedding dynamics. The validation exercise thus provides a useful baseline for interpreting the tandem-cylinder results presented in the following sections.

4. Results and Discussion

The flow characteristics around two cylinders arranged in tandem are analysed at a Reynolds number of $Re = 1.0 \times 10^5$ using the Reynolds-averaged Navier–Stokes (RANS) approach with the standard k–ε turbulence model. The key flow parameters employed in the simulations are summarised in Table 4. The chosen Reynolds number corresponds to a turbulent flow regime in which strong vortex shedding, wake interaction, and complex unsteady flow structures are expected.

Table 4. Flow parameters.

Parameter	Value
Freestream velocity U_∞ (m/s)	1.0
Kinematic viscosity ν (m^2/s)	1.0×10^{-6} (water)
Reynolds number $Re = U_\infty D_1/\nu$	1.0×10^5
Turbulence intensity at inlet	5%
Time step Δt (s)	0.001
Total simulation time (s)	10

As shown in Table 4, the inlet velocity is fixed at $U_\infty = 1$ m/s, and the fluid properties correspond to water, yielding a high Reynolds number flow. Under these conditions, the flow is fully turbulent and characterised by significant inertial effects relative to viscous forces. The imposed turbulence intensity of 5% ensures realistic inflow conditions, promoting the development of turbulent structures downstream of the cylinders.

The selected time step, $\Delta t = 0.001$ s, is sufficiently small to resolve the transient evolution of the flow and capture vortex shedding phenomena with reasonable temporal accuracy. The total simulation time of 10 s allows the flow to reach a statistically steady state, enabling meaningful computation of time-averaged quantities such as drag, lift, and Strouhal number.

4.1. Flow Field Visualisation

The transient evolution of the velocity field around the tandem cylinders is shown in Figure 4. At the initial stage ($t = 0$, Figure 4a), the flow remains nearly uniform due to the potential flow initialisation. As time progresses to $t = 1$s (Figure 4b), flow separation begins to develop around both cylinders, leading to the formation of small recirculation zones. At later times, $t = 5$s and $t = 10$s (Figures 4c and 4d), a fully developed wake is observed, characterised by low-velocity regions behind the cylinders and accelerated flow around their surfaces. The wake interaction between the upstream and downstream cylinders becomes clearly visible, indicating strong hydrodynamic coupling.

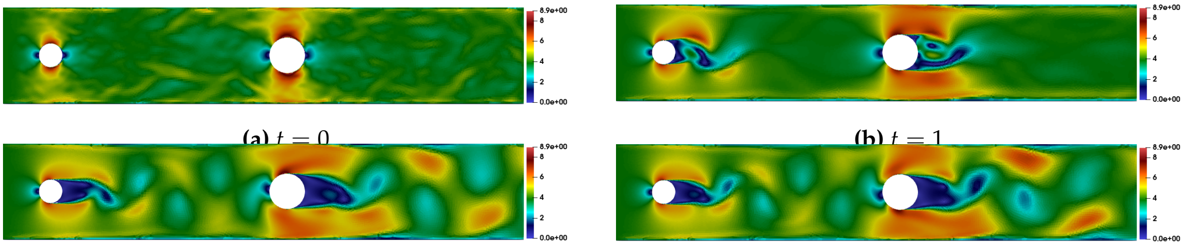

(a) $t = 0$ (b) $t = 1$

(c) $t = 5$ (d) $t = 10$

Figure 4. Temporal evolution of the velocity magnitude U around the tandem cylinders.

The distribution of turbulent kinetic energy is presented in Figure 5. At $t = 0$ (Figure 5a), turbulence levels are negligible. As the flow develops ($t = 1$s, Figure 5b), shear layers form around the cylinders, increasing turbulence production. At $t = 5$s and $t = 10$s (Figures 5c and 5d), high values of k are concentrated in the shear layers and wake regions, especially in the interaction zone between the two cylinders, indicating strong energy transfer from the mean flow to turbulent fluctuations.

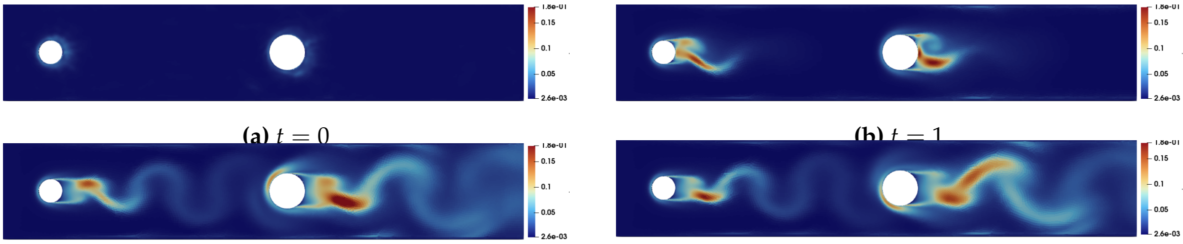

(a) $t = 0$ (b) $t = 1$

(c) $t = 5$ (d) $t = 10$

Figure 5. Temporal evolution of the turbulent kinetic energy k around the tandem cylinders.

The evolution of the turbulence dissipation rate is shown in Figure 6. Initially ($t = 0$, Figure 6a), ϵ remains very low throughout the domain. As vortical structures develop ($t = 1$s, Figure 6b), localised dissipation regions appear near the cylinder surfaces. At later times ($t = 5$s and $t = 10$s, Figures 6c and 6d), the dissipation rate is highly concentrated in the shear layers and wake regions, indicating the breakdown of turbulent eddies into smaller scales.

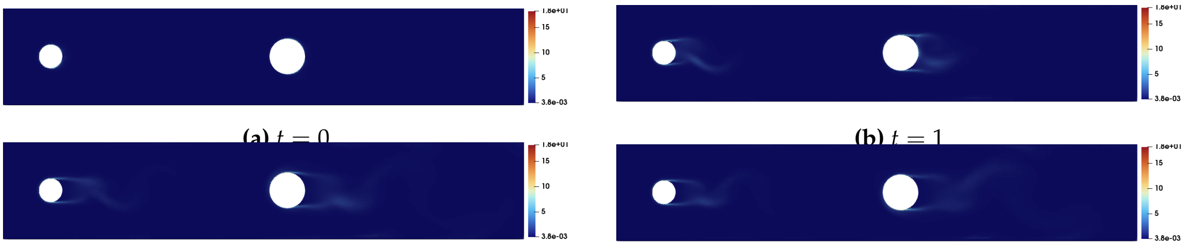

(a) $t = 0$ (b) $t = 1$

(c) $t = 5$ (d) $t = 10$

Figure 6. Temporal evolution of the turbulence dissipation rate ϵ around the tandem cylinders.

The pressure field evolution is illustrated in Figure 7. At $t = 0$ (Figure 7a), the pressure distribution is nearly symmetric. As the flow develops ($t = 1$s, Figure 7b), a high-pressure region forms at the upstream stagnation points of the cylinders, while low-pressure regions develop in their wakes. At later times ($t = 5$s and $t = 10$s, Figures 7c and 7d), the pressure field becomes asymmetric due to vortex shedding and wake interaction, particularly affecting the downstream cylinder.

Preprints.org (www.preprints.org) | NOT PEER-REVIEWED | Posted: 24 March 2026 doi:10.20944/preprints202603.1921.v1

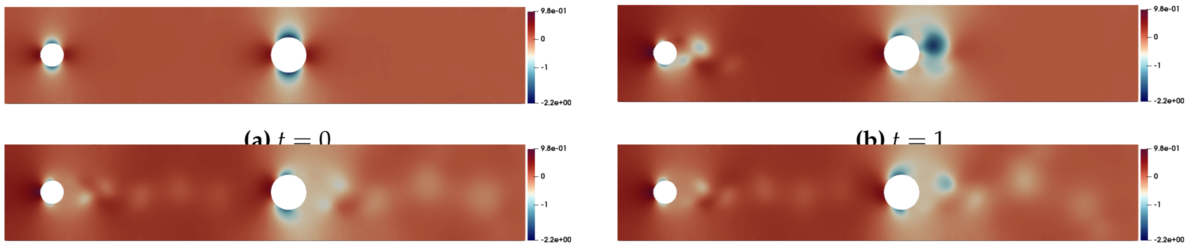

(a) $t = 0$ (b) $t = 1$

(c) $t = 5$ (d) $t = 10$

Figure 7. Temporal evolution of the pressure field p around the tandem cylinders.

4.2. Line Profiles

The variation of the velocity magnitude at a selected downstream location is shown in Figure 8. The profile clearly reflects the influence of the wake generated by the upstream and downstream cylinders. A significant velocity deficit is observed in the central region of the channel, corresponding to the wake zone, while higher velocities appear near the upper and lower walls due to flow acceleration around the cylinders. This non-uniform distribution indicates strong momentum loss in the wake and recovery toward the free-stream velocity away from the centreline.

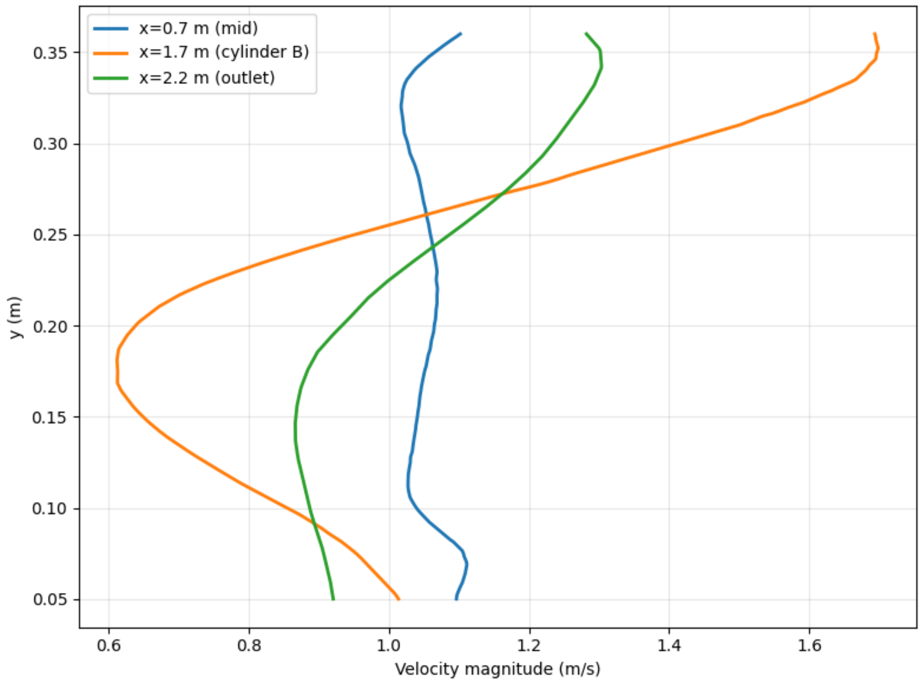

Figure 8. Velocity magnitude profile at a selected downstream location.

The turbulent kinetic energy distribution at the same location is presented in Figure 9. The profile shows peak values in regions corresponding to strong shear layers, particularly near the wake boundaries. The elevated turbulence levels indicate intense mixing and energy transfer from the mean flow to turbulent fluctuations. Lower values of k are observed away from the wake, where the flow becomes more uniform.

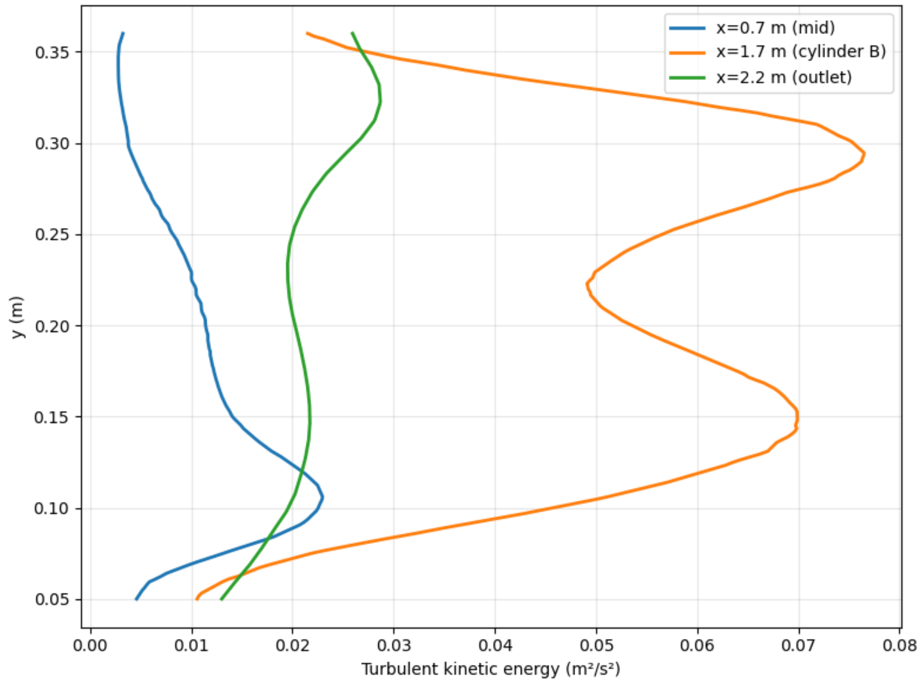

Figure 9. Turbulent kinetic energy profile at a selected downstream location.

The dissipation rate profile is shown in Figure 10. Similar to the turbulent kinetic energy, ϵ attains higher values in the shear layer regions where turbulent eddies break down into smaller scales. The peaks in ϵ indicate zones of strong viscous dissipation, while lower values away from the wake region suggest reduced turbulent activity.

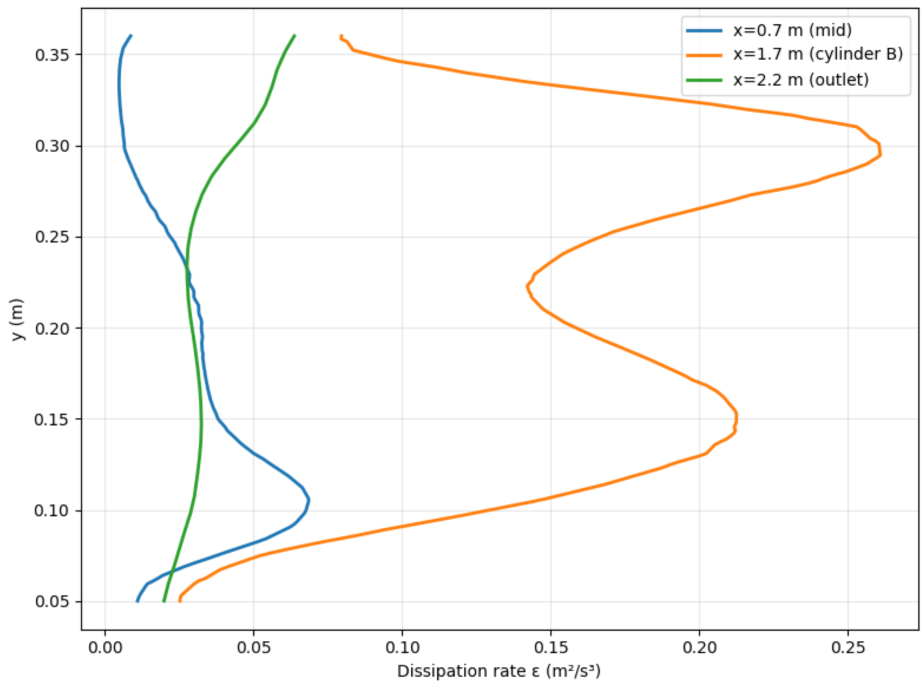

Figure 10. Dissipation rate ϵ profile at a selected downstream location.

The turbulent viscosity distribution is illustrated in Figure 11. The profile shows increased turbulent viscosity in the wake and shear layer regions, where turbulence intensity is high. This enhanced viscosity reflects the increased momentum transport due to turbulent mixing. In contrast,

Preprints.org (www.preprints.org) | NOT PEER-REVIEWED | Posted: 24 March 2026 doi:10.20944/preprints202603.1921.v1

near-wall and free-stream regions exhibit lower turbulent viscosity, indicating weaker turbulence effects.

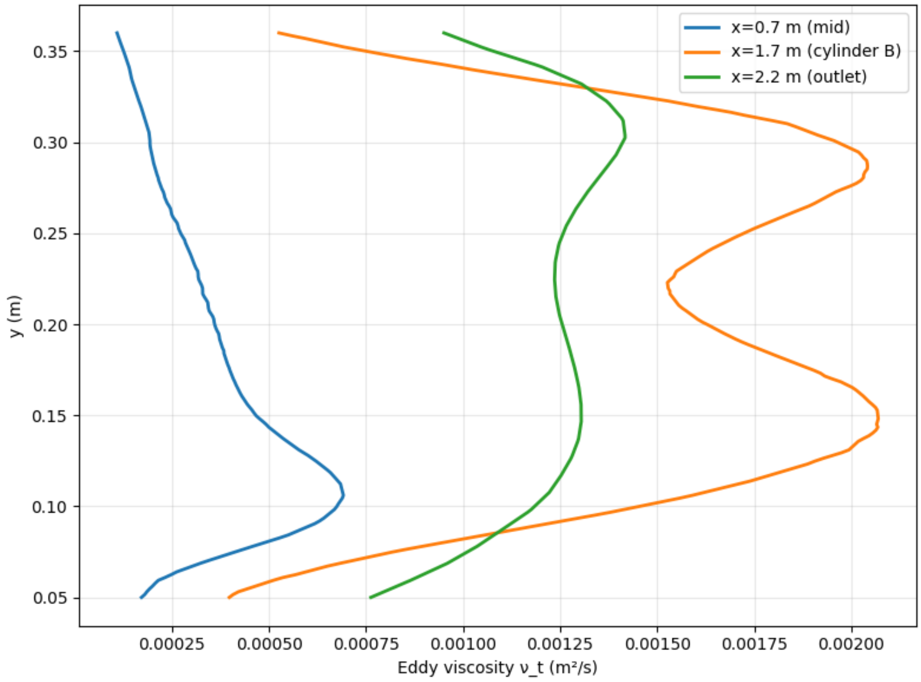

Figure 11. Turbulent viscosity distribution at a selected downstream location.

The pressure distribution at the selected location is shown in Figure 12. The profile indicates a pressure deficit in the wake region due to flow separation and vortex shedding. Away from the wake, the pressure gradually recovers toward the free-stream value. The asymmetry in the pressure distribution reflects the unsteady nature of the wake and its interaction with the downstream cylinder.

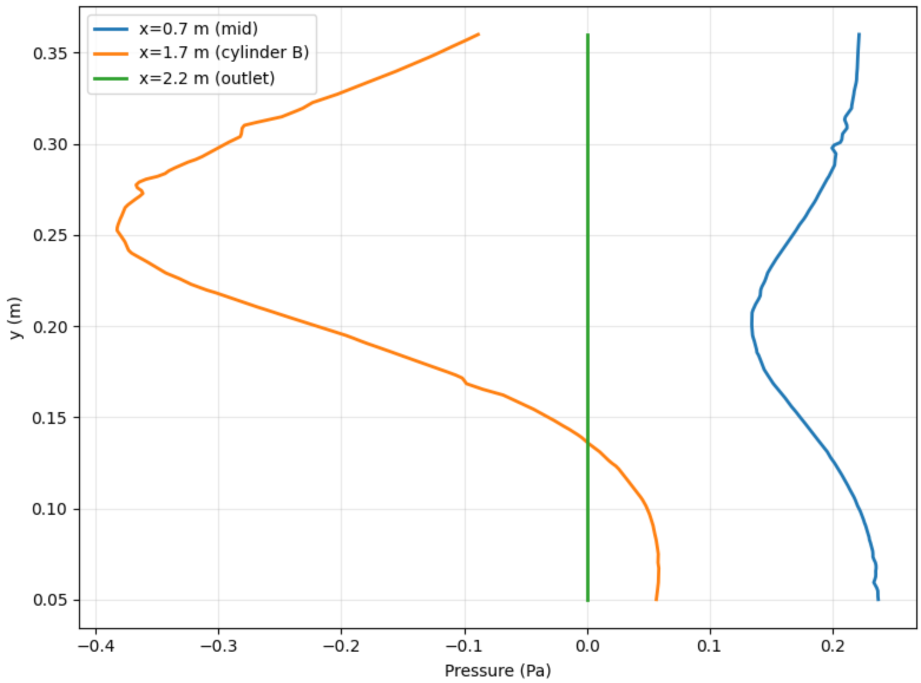

Figure 12. Pressure profile at a selected downstream location.

 doi:10.20944/preprints202603.1921.v1

4.3. Force Coefficients and Vortex Shedding

The time-averaged drag coefficient and the roo -mean-square (RMS) lift coefficient for both cylinders are reported in Table 5. The upstream cylinder (A) shows a mean drag coefficient of $\overline{C_D} = 0.947$, whereas the downstream cylinder (B) has a slightly larger value of $\overline{C_D} = 0.997$. This increase indicates that the downstream cylinder experiences a stronger net resistance due to its exposure to the unsteady wake of the upstream cylinder.

The RMS lift coefficient is much smaller for the upstream cylinder, $C_L' = 0.129$, than for the downstream cylinder, $C_L' = 0.340$. This clearly shows that the downstream cylinder is subjected to stronger lateral unsteadiness and more intense vortex-induced loading. In tandem-cylinder configurations, the wake of the first cylinder typically impinges on the second cylinder, amplifying the lift fluctuations and making the downstream body more sensitive to flow oscillations.

Table 5. Time-averaged drag and RMS lift coefficients.

Cylinder	$\overline{C_D}$	C_L' (RMS)
A (upstream)	0.947	0.129
B (downstream)	0.997	0.340

The temporal variation of the drag and lift coefficients is shown in Figure 13. The plot indicates an initial transient stage, during which both coefficients adjust from the starting condition toward a periodic or statistically periodic regime. After this initial adjustment, the drag coefficient exhibits comparatively weaker oscillations than the lift coefficient, which is consistent with bluff-body wake dynamics. The lift history contains stronger fluctuations because the alternating shedding of vortices produces an unsteady transverse force on the cylinders.

For the upstream cylinder, the oscillations are relatively moderate because it interacts primarily with the incoming flow. For the downstream cylinder, however, the amplitude of the lift oscillation is larger, reflecting the effect of wake interference and the stronger unsteady forcing imposed by the upstream cylinder's shed vortices. Overall, the force histories confirm that the downstream cylinder experiences a more vigorous unsteady aerodynamic loading than the upstream cylinder.

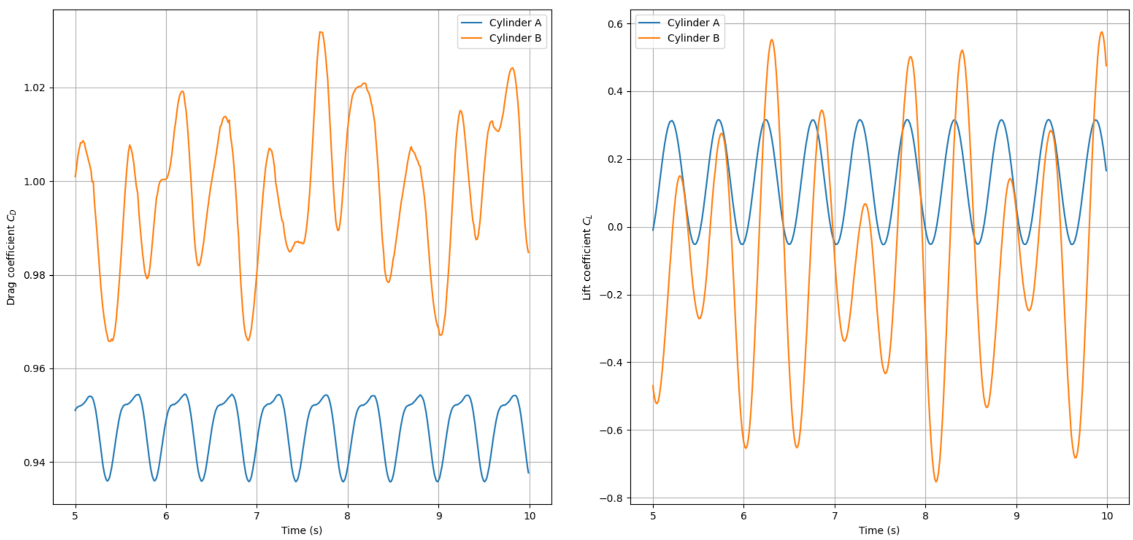

Figure 13. Temporal variation of the drag and lift coefficients for the tandem cylinders.

The vortex shedding characteristics of the tandem cylinders are summarised in Table 6. Both cylinders exhibit the same dominant shedding frequency, $f = 6.443$ Hz, indicating that the wake interaction causes a common unsteady shedding mode in the system. However, the corresponding

Preprints.org (www.preprints.org) | NOT PEER-REVIEWED | Posted: 24 March 2026 doi:10.20944/preprints202603.1921.v1

Strouhal numbers are different because they are based on different characteristic diameters. The upstream cylinder (A) has $St = 0.644$, while the downstream cylinder (B) has a higher value of $St = 0.966$. This difference suggests that the downstream cylinder responds more strongly to the upstream wake and experiences a more rapid non-dimensional shedding behaviour.

Table 6. Strouhal numbers and shedding frequencies.

Cylinder	Frequency f (Hz)	Strouhal number St
A (upstream)	6.443	0.644
B (downstream)	6.443	0.966

The frequency spectrum of the lift coefficient is shown in Figure 14. A clear dominant peak appears at the shedding frequency, confirming that the lift fluctuations are governed by a periodic vortex-shedding mechanism. The presence of a strong spectral peak indicates that the flow has reached a quasi-periodic state after the initial transient stage. Since the downstream cylinder is directly exposed to the wake of the upstream cylinder, its lift response is expected to contain stronger unsteady components, which is consistent with the larger RMS lift reported in Table 5. Overall, the FFT results confirm the existence of coherent oscillatory motion in the wake and provide a reliable estimate of the shedding frequency used to compute the Strouhal number.

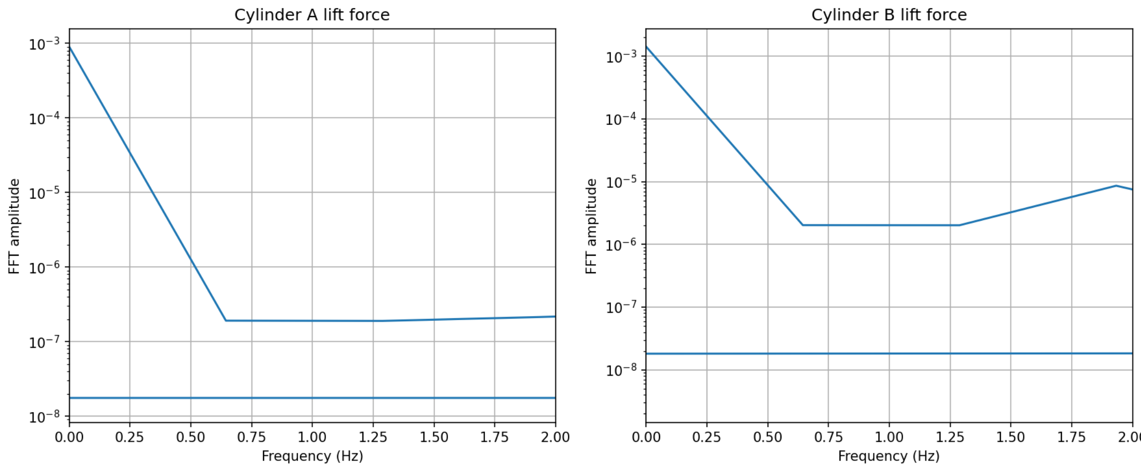

Figure 14. Frequency spectrum of the lift coefficient showing the dominant vortex-shedding frequency.

4.4. Probe Statistics and Time Histories

The statistical quantities extracted at the two probe locations are summarised in Table 7. Probe 0, located at $(1.5, 0.2, 0.005)$, lies closer to the near-wake region and therefore records a lower mean velocity magnitude, $U_{\text{mag}} = 0.236$ m/s, with comparatively strong fluctuations. Probe 1, at $(1.8, 0.2, 0.005)$, is farther downstream and shows a much larger mean velocity magnitude of 0.791 m/s, indicating partial recovery of the flow toward the free-stream condition. The RMS values suggest that unsteady velocity fluctuations remain significant at both points, with probe 1 exhibiting a slightly larger velocity fluctuation level than probe 0. For pressure, both probes record negative mean values, which is consistent with the low-pressure wake behind the cylinders. The more negative mean pressure at probe 1 indicates that it is more strongly influenced by the downstream wake structure.

 doi:10.20944/preprints202603.1921.v1

Table 7. Mean and RMS values at the two probe locations.

Probe	Location (x, y, z)	Quantity	Mean	RMS
0	(1.5, 0.2, 0.005)	U_{mag} (m/s)	0.236	0.155
		p (Pa)	-0.089	0.201
1	(1.8, 0.2, 0.005)	U_{mag} (m/s)	0.791	0.211
		p (Pa)	-0.162	0.180

The time history of the streamwise velocity component at the probe locations is shown in Figure 15. The signal exhibits clear unsteady oscillations, reflecting the periodic passage of vortices in the wake. The fluctuation amplitude is larger at the downstream probe, which indicates that the wake-induced unsteadiness persists farther downstream and remains dynamically important.

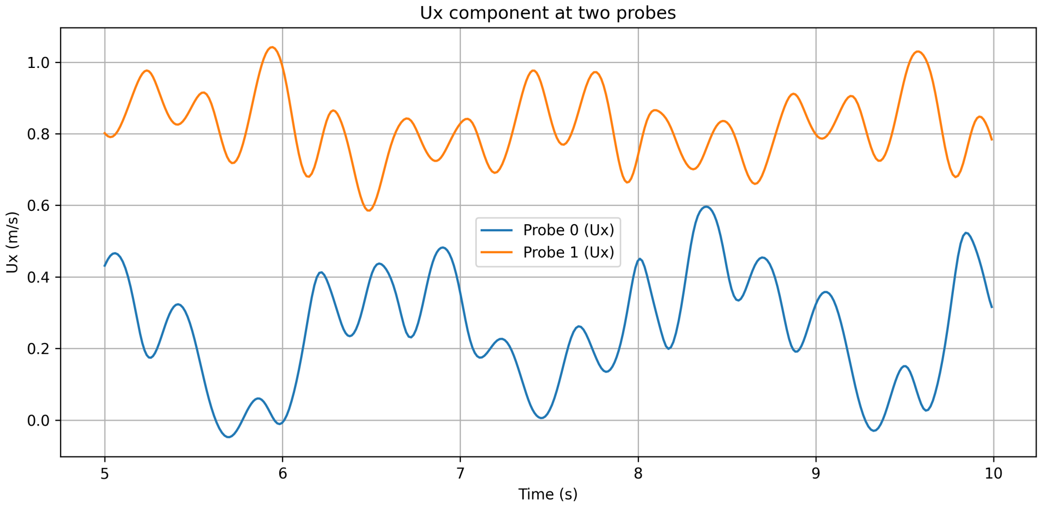

Figure 15. Temporal variation of the streamwise velocity component at the probe locations.

The cross-stream velocity component is presented in Figure 16. Compared with the streamwise component, the cross-stream signal is typically more sensitive to vortex shedding because it directly reflects the alternating lateral motion of the wake. The oscillatory pattern confirms the presence of a strong periodic transverse flow caused by the unsteady separation behind the tandem cylinders.

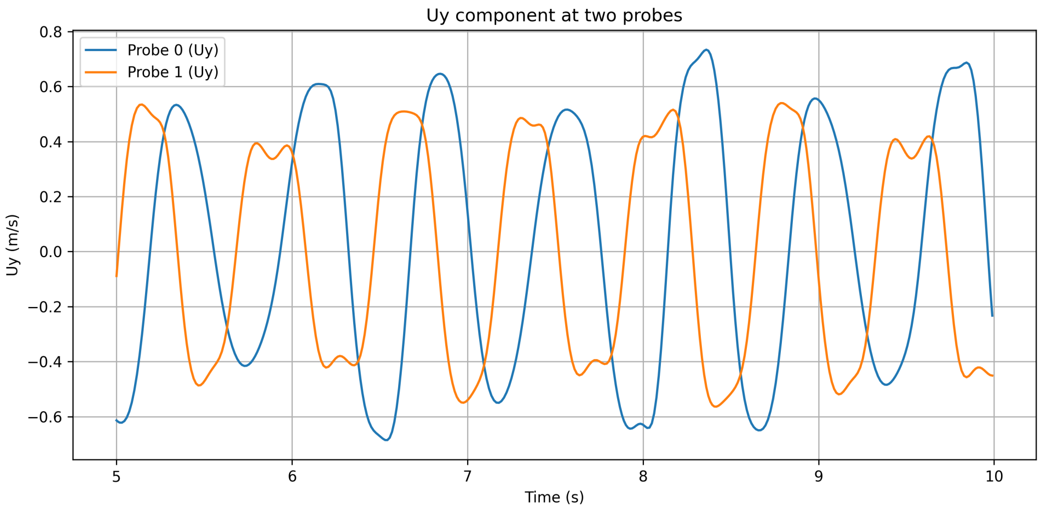

Figure 16. Temporal variation of the cross-stream velocity component at the probe locations.

Preprints.org (www.preprints.org) | NOT PEER-REVIEWED | Posted: 24 March 2026 doi:10.20944/preprints202603.1921.v1

The pressure histories at the same probe points are shown in Figure 17. The pressure fluctuates periodically due to the alternating vortex shedding and the associated wake development. The amplitude of the pressure variation is substantial, especially near the wake region, which confirms that pressure unsteadiness plays a major role in the aerodynamic loading on the cylinders. Together, Figures 15–17 demonstrate that both velocity and pressure remain strongly time-dependent in the downstream wake, consistent with the force fluctuations reported earlier.

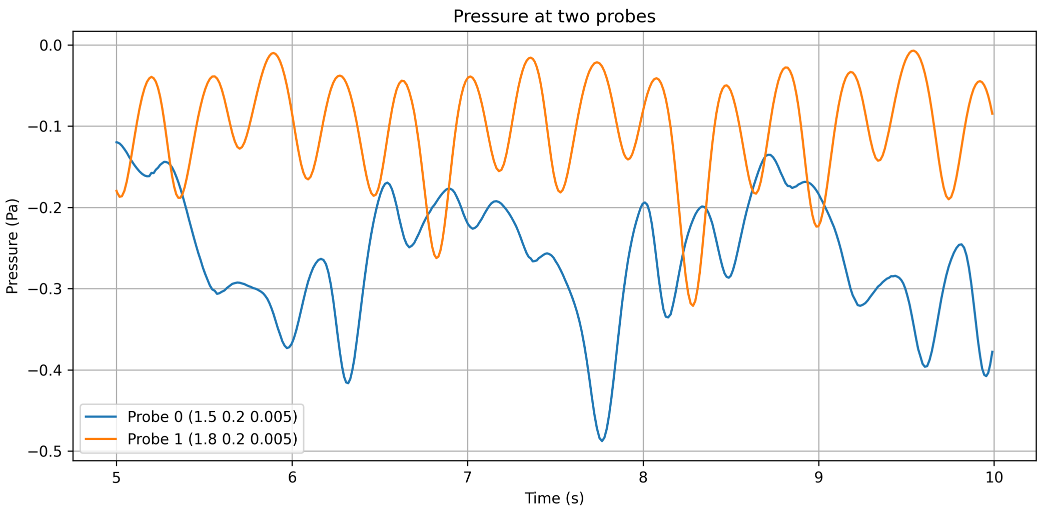

Figure 17. Temporal variation of pressure at the probe locations.

5. Conclusion

This study presented a numerical investigation of the flow past two cylinders in tandem arrangement using open-source tools. The complete workflow from mesh generation with Gmsh to finite-volume simulation with OpenFOAM was described in detail, providing a fully reproducible methodology for bluff-body flow problems.

The numerical setup was first validated against the classical Schäfer–Turek single-cylinder benchmark at $Re = 100$. The maximum drag coefficient ($C_{D,\max} = 3.158$) and the dominant shedding frequency ($St = 0.262$) showed reasonable agreement with the reference data, confirming the solver's ability to capture the essential vortex-shedding features. The small discrepancies in mean drag and lift were attributed to differences in inlet profile and mesh resolution, which were acceptable for the purpose of this study.

The main investigation focused on the tandem-cylinder configuration at $Re = 1.0 \times 10^5$. The flow was fully turbulent, with strong vortex shedding and wake interaction. Visualisation of the instantaneous fields revealed that the upstream cylinder (A) generates a periodic wake that impinges on the downstream cylinder (B), leading to amplified unsteady loading on the latter. The time-averaged drag coefficients were $\overline{C}_D = 0.947$ for cylinder A and $\overline{C}_D = 0.997$ for cylinder B, while the RMS lift coefficients were $C_L' = 0.129$ and $C_L' = 0.340$, respectively. The downstream cylinder thus experienced higher net drag and significantly larger lift fluctuations, consistent with wake interference.

Both cylinders shed vortices at the same frequency ($f = 6.443$ Hz), yielding Strouhal numbers $St = 0.644$ for cylinder A (based on its diameter) and $St = 0.966$ for cylinder B. The spectral analysis of the lift coefficient confirmed a clear dominant peak, indicating a well-established periodic shedding regime.

Quantitative profiles extracted downstream of the cylinders showed a pronounced velocity deficit in the wake, with partial recovery farther downstream. Turbulent kinetic energy, dissipation rate, and eddy viscosity peaked in the shear layers and wake regions, highlighting strong turbulence production and mixing. Pressure profiles exhibited a notable deficit in the wake, consistent with the low-pressure region behind the cylinders.

Preprints.org (www.preprints.org) | NOT PEER-REVIEWED | Posted: 24 March 2026 doi:10.20944/preprints202603.1921.v1

Probe data at two downstream locations ($(1.5, 0.2, 0.005)$ and $(1.8, 0.2, 0.005)$) revealed that both streamwise and cross-stream velocity components, as well as pressure, remained highly unsteady, with the downstream probe showing larger fluctuations. These data provide a quantitative reference for wake dynamics.

This work demonstrates that an open-source CFD pipeline can successfully simulate complex turbulent flow around tandem cylinders. The results offer detailed insights into wake interaction, force coefficients, and turbulence characteristics, serving as a benchmark for future studies. The methodology is freely available and can be readily adapted to similar bluff-body problems.

Future work could extend the analysis to different Reynolds numbers, cylinder spacings, or incorporate more advanced turbulence models such as LES or DES to capture finer-scale turbulent structures. A systematic mesh convergence study would further refine the accuracy of force predictions. The open-source nature of the tools ensures that such extensions can be easily implemented and shared within the research community.

Nomenclature

Table 8. List of symbols.

Symbol	Description	Units
u_i	Velocity component	$\mathrm{m\,s^{-1}}$
$\overline{u_i}$	Mean velocity component	$\mathrm{m\,s^{-1}}$
p	Pressure	Pa
$\overline{p}$	Mean pressure	Pa
ρ	Density	$\mathrm{kg\,m^{-3}}$
ν	Kinematic viscosity	$\mathrm{m^2\,s^{-1}}$
ν_t	Turbulent (eddy) viscosity	$\mathrm{m^2\,s^{-1}}$
k	Turbulent kinetic energy	$\mathrm{m^2\,s^{-2}}$
ε	Turbulent dissipation rate	$\mathrm{m^2\,s^{-3}}$
$C_\mu, C_{\varepsilon 1}, C_{\varepsilon 2}, \sigma_k, \sigma_\varepsilon$	Model constants	–
κ	von Kármán constant	–
E	Roughness parameter	–
y^+	Dimensionless wall distance	–
D_1, D_2	Diameters of upstream and downstream cylinders	m
L	Channel length	m
H	Channel height	m
t	Extruded thickness	m
U_∞	Freestream velocity	$\mathrm{m\,s^{-1}}$
Re	Reynolds number	–
St	Strouhal number	–
f	Vortex shedding frequency	Hz
C_D	Drag coefficient	–
C_L	Lift coefficient	–
$\overline{C_D}$	Mean drag coefficient	–
C_L'	RMS lift coefficient	–

References

1. King, R. A review of vortex shedding research and its application. *Ocean Engineering* **1977**, *4*, 141–171.
2. Williamson, C. K. Vortex dynamics in the cylinder wake. *Annual Review of Fluid Mechanics* **1996**, *28*, 477–539.
3. Norberg, C. Flow around a circular cylinder: aspects of fluctuating lift. *Journal of fluids and structures* **2001**, *15*, 459–469.
4. Zdravkovich, M. Review of flow interference between two circular cylinders in various arrangements **1977**.
5. Sumner, D. Two circular cylinders in cross-flow: A review. *Journal of fluids and structures* **2010**, *26*, 849–899.
6. Zhang, X.F.; Yang, J.C.; Ni, M.J.; Zhang, N.M.; Yu, X.G. Experimental and numerical studies on the three-dimensional flow around single and two tandem circular cylinders in a duct. *Physics of Fluids* **2022**, *34*.

doi:10.20944/preprints202603.1921.v1

7. Wang, X.; Zhang, J.X.; Hao, Z.; Zhou, B.; Tan, S. Influence of wall proximity on flow around two tandem circular cylinders. *Ocean Engineering* **2015**, *94*, 36–50.
8. Khan, H.H.; Islam, M.D.; Fatt, Y.Y.; Janajreh, I.; Alam, M.M. Flow-induced vibration on two tandem cylinders of different diameters and spacing ratios. *Ocean Engineering* **2022**, *258*, 111747.
9. Schäfer, M.; Turek, S.; Durst, F.; Krause, E.; Rannacher, R. Benchmark computations of laminar flow around a cylinder. In *Flow simulation with high-performance computers II: DFG priority research programme results 1993–1995*; Springer, 1996; pp. 547–566.
10. Vu, H.C.; Ahn, J.; Hwang, J.H. Numerical simulation of flow past two circular cylinders in tandem and side-by-side arrangement at low Reynolds numbers. *KSCE Journal of Civil Engineering* **2016**, *20*, 1594–1604.
11. Jiang, H.; Cheng, L.; Draper, S.; An, H. Two-and three-dimensional instabilities in the wake of a circular cylinder near a moving wall. *Journal of Fluid Mechanics* **2017**, *812*, 435–462.
12. Liang, C.; Papadakis, G. Large eddy simulation of pulsating flow over a circular cylinder at subcritical Reynolds number. *Computers & fluids* **2007**, *36*, 299–312.
13. Elgendy, A.M. NUMERICAL INVESTIGATION OF CROSS-FLOW OVER OSCILLATING TANDEM CYLINDERS WITH TWO DEGREES OF FREEDOM. PhD thesis, Khalifa University of Science, 2024.
14. Xu, W.; Wu, H.; Jia, K.; Wang, E. Numerical investigation into the effect of spacing on the flow-induced vibrations of two tandem circular cylinders at subcritical Reynolds numbers. *Ocean Engineering* **2021**, *236*, 109521.
15. Zhao, M.; Mamoon, A.A.; Wu, H. Numerical study of the flow past two wall-mounted finite-length square cylinders in tandem arrangement. *Physics of fluids* **2021**, *33*.
16. Chang, X.; Yin, P.; Xin, J.; Shi, F.; Wan, L. Wake structures and hydrodynamic characteristics of flows around two near-wall cylinders in tandem and parallel arrangements. *Journal of Marine Science and Engineering* **2024**, *12*, 832.
17. Nguyen, Q.D.; Lu, W.; Chan, L.; Ooi, A.; Lei, C. A state-of-the-art review of flows past confined circular cylinders. *Physics of Fluids* **2023**, *35*.
18. Vu, V.T.; Duong, V.D.; Ngo, I.L. A comprehensive study of low-Reynold flow through two tandem cylinders with various configurations using the Lattice Boltzmann method. *Marine Geophysical Research* **2025**, *46*, 7.
19. Kumar, R.A.; Kumar, K.S.; et al. Numerical Investigation of Wake Interference in Tandem Square Cylinders at Low Reynolds Numbers. *Symmetry* **2025**, *17*, 2038.
20. Wang, J.; Shan, X.; Liu, J. First instability of the flow past two tandem cylinders with different diameters. *Physics of Fluids* **2022**, *34*.
21. Zhang, L.; Zhang, Z.; Chen, W.; Srinil, N.; Zhu, H.; Bao, Y.; Ji, C. Flow-induced vibrations of ten tandem cylinders at low Reynolds number. *Physics of Fluids* **2023**, *35*.
22. Sarkar, S.; Gupta, N.; Debnath, K.; Lawrence Raj, P.R. Computational Analysis of Flow Around Two Wall-Mounted Trapezoidal Bluff Bodies Arranged in Tandem Position. *Journal of Fluids Engineering* **2025**, *147*, 021301.
23. Zhao, F.; Wang, R.; Zhu, H.; Cao, Y.; Bao, Y.; Zhou, D.; Cheng, B.; Han, Z. Free-surface effects on the flow around two circular cylinders in tandem. *Journal of Fluid Mechanics* **2024**, *1001*, A7.
24. Geuzaine, C.; Remacle, J.F. *Gmsh: A Three-Dimensional Finite Element Mesh Generator*, 2025. Version 4.12.
25. Launder, B.E.; Spalding, D.B. The numerical computation of turbulent flows. *Computer Methods in Applied Mechanics and Engineering* **1974**, *3*, 269–289.